Design and Signature Analysis of Remote Trace-Gas Identification Methodology Based on Infrared-Terahertz Double-Resonance Spectroscopy

Elizabeth A. Tanner,[1] Dane J. Phillips,[1] Christopher M. Persons,[1] Frank C. De Lucia,[2] and Henry O. Everitt[3,4,*]

[1]*IERUS Technologies, 2904 Westcorp Boulevard, Suite 210, Huntsville, Alabama 35805, USA*
[2]*Department of Physics, 191 Woodruff Avenue, The Ohio State University, Columbus, Ohio 43210, USA*
[3]*Charles M. Bowden Laboratory, Army Aviation & Missile RD&E Center, Redstone Arsenal, Alabama 35898, USA*
[4]*Department of Physics, Duke University, Durham, North Carolina 27708, USA*

(Received 24 April 2014; revised manuscript received 30 September 2014; published 26 November 2014)

The practicality of a newly proposed infrared-terahertz (IR-THz) double-resonance (DR) spectroscopic technique for remote trace-gas identification is explored. The strength of the DR signatures depends on known molecular parameters from which a combination of pump-probe transitions may be identified to recognize a specific analyte. Atmospheric pressure broadening of the IR and THz trace-gas spectra relaxes the stringent pump coincidence requirement, allowing many DR signatures to be excited, some of which occur in the favorable atmospheric transmission windows below 500 GHz. By designing the DR spectrometer and performing a detailed signal analysis, the pump-probe power requirements for detecting trace amounts of methyl fluoride, methyl chloride, or methyl bromide may be estimated for distances up to 1 km. The strength of the DR signature increases linearly with pump intensity but only as the square root of the probe power because the received signal is in the Townes noise limit. The concept of a specificity matrix is introduced and used to quantify the recognition specificity and calculate the probability of false positive detection of an interferent.

DOI: 10.1103/PhysRevApplied.2.054016

I. INTRODUCTION

Infrared (IR) spectroscopic techniques are widely used for atmospheric molecular analysis [1–3], discrimination, and remote sensing applications [4,5]. The spectra measured by IR remote sensing techniques are associated with vibrational modes of constituent intramolecular bonds that must be interpreted in order to identify the analyte. By contrast, molecular rotational spectroscopy in the terahertz (THz)-frequency region reliably identifies the composition in most low-pressure gas mixtures [6], but its detection and recognition specificity at atmospheric pressures is greatly reduced by pressure broadening of the spectral features [7]. A remote sensing methodology based on IR-THz double-resonance (DR) spectroscopy has been recently shown to overcome these limitations by achieving precise molecular recognition specificity, even discriminating isotopomers, at distances up to 1 km [7,8].

Gas-phase molecular double-resonance techniques have been widely used in optical spectroscopy to investigate collisional energy transfer [9–11], but the applicability of IR-THz DR techniques has been limited by the rarity of IR-frequency coincidences between pump CO_2 laser lines and absorbing molecular rotational-vibrational transitions at the low pressures used for collisional energy transfer studies [12–14]. Indeed, the specificity of our DR technique depends on the rarity of such coincidences and the associated idiosyncrasies of a specific molecule's rotational and vibrational spectra. Although additional coincidences emerge at atmospheric pressure because of the increased collisional linewidths, this can be an advantage if some of the additional coincidences produce DR signatures within more favorable THz propagation windows [15–18].

This DR spectroscopic technique uses a pulsed CO_2 pump laser to create transient nonequilibrium population distributions among rotational energy states. The infrared laser frequency is tuned to coincide with a specific rotational-vibrational transition connecting states with rotational quantum numbers J_L and J_U. Absorption of pump photons transfers population from the heavily populated state L in the ground vibrational level to the sparcely populated state U in an excited vibrational level. Pump-induced deviation from equilibrium population conditions modifies the absorption coefficient of the terahertz-frequency rotational transitions connected to these states, producing enhanced absorption for the $J_L - 1 \rightarrow J_L$ and $J_U \rightarrow J_U + 1$ transitions and reduced absorption for the $J_L \rightarrow J_L + 1$ and $J_U - 1 \rightarrow J_U$ transitions (Fig. 1). A continuous-wave (cw) probe beam is tuned to coincide with one of these rotational transitions such that laser-modulated absorption strength is detected as a temporal variation in transmitted probe power synchronized with the laser pulses.

*Corresponding author.
everitt@phy.duke.edu

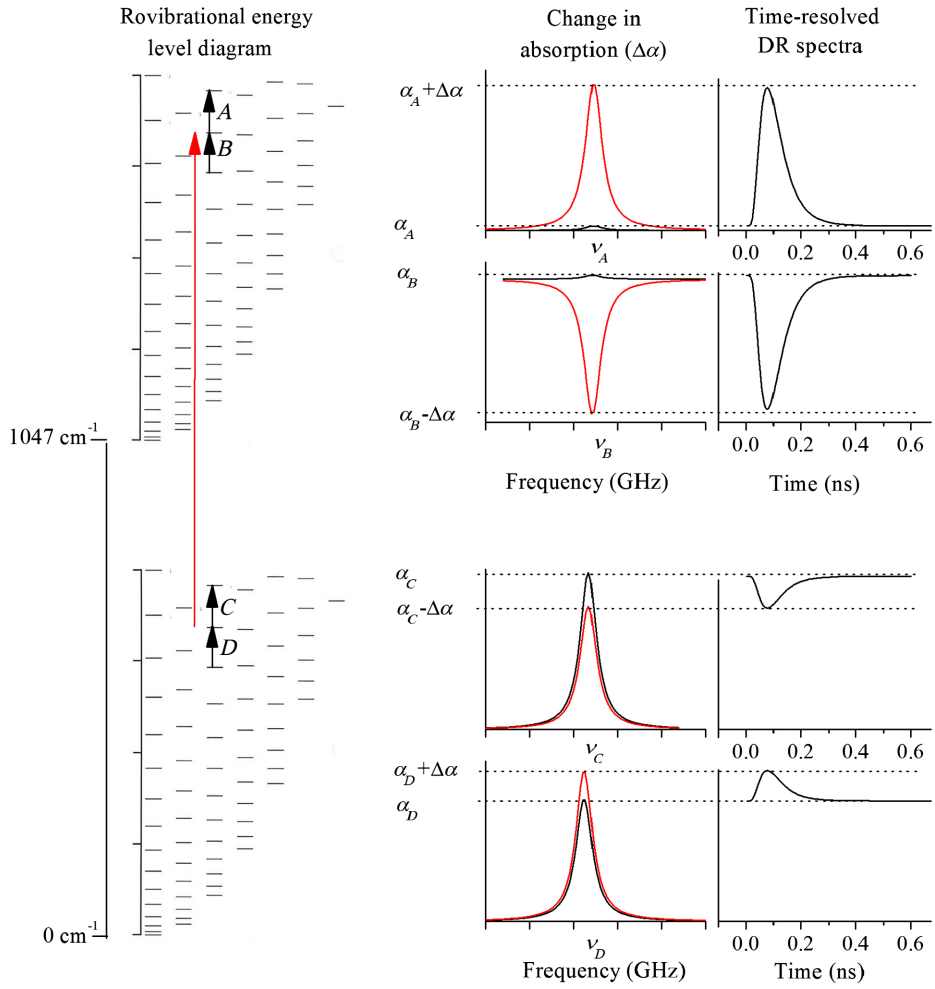

FIG. 1 Schematic energy level diagram illustrating the DR remote sensing concept and the corresponding spectral and temporal evolution of the DR signal.

Here we explore a methodology by which the optimal pump and probe frequencies may be identified for a given molecular analyte based on a combination of molecule-specific "laboratory" spectroscopy and scenario-dependent atmospheric conditions. The dependence of the DR signature's signal-to-noise ratio (SNR) on the power of copropagating pump-probe beams is also quantitatively estimated, the latter of which is monitored via reflection from a cooperative corner-cube retroreflector placed up to 1 km from the transceiver [Fig. 2(a)]. These calculations firmly establish the feasibility of this new remote sensing methodology, identify the minimal hardware performance requirements needed for a DR-based sensor to operate in various atmospheric conditions, and specify how to select optimal DR signatures for remotely identifying the constituents of a trace molecular cloud (<100 ppm m). The concept of a specificity matrix is introduced by which the recognition specificity and the probability of false positive detection of an interferent are quantitatively estimated.

II. HARDWARE-SPECIFIC SOURCES OF NOISE

We begin by identifying and quantifying the noise in the probe receiver. DR spectroscopy requires the sensitive detection of a small ($\ll$1%) temporal (<0.5 ns) change in a much larger background probe signal. A heterodyne detection approach in which the received probe signal is mixed with a local oscillator and amplified after down-conversion can provide the most sensitive detection and amplification of the modulated DR signal [Fig. 2(b)]. Four sources of noise must be considered: $1/f$ or flicker noise, blackbody radiation noise, noise from the mixers and amplifiers, and Townes noise. Of these four, $1/f$ noise can be easily minimized at the front end by choosing a high intermediate frequency (IF > 100 MHz) and at the back end by choosing appropriate integration times and signal summation strategies [19]. In a Schottky-diode-based heterodyne system, blackbody noise is manifested through the bandwidth of the detectors and the mode matching required to couple radiation into these detectors efficiently.

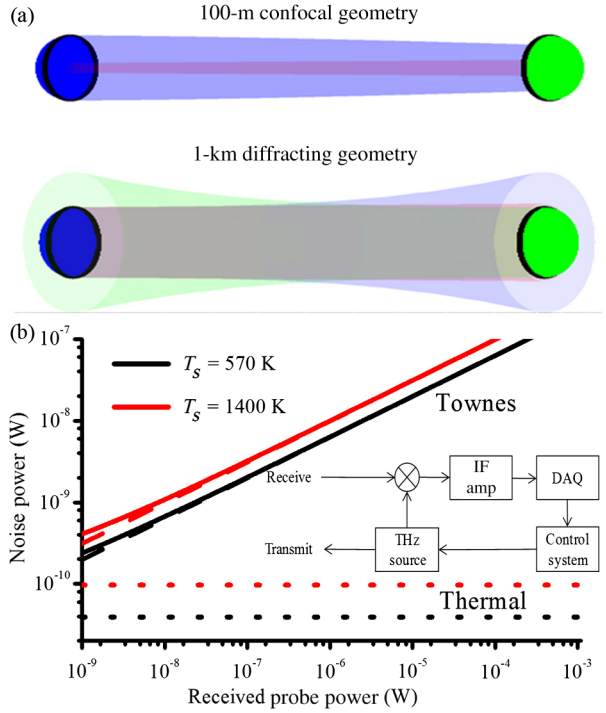

FIG. 2 (a) Schematic diagram of the 100-m confocal and 1-km diffracting probe architecture for the DR chemical sensor. The red beam is the IR pump, and the blue and green beams are the transmitted and reflected THz probe from the respective antenna and retroreflector. (b) The dependence of noise power on probe power received at the detector for $b = B = 5$ GHz for the extremes in system noise temperature T_S. The inset presents a notional diagram of the THz transceiver.

In the long-wavelength limit, the blackbody thermal noise may be approximated by [20]

$$P_{\rm th} \approx kT(bB)^{1/2}, \tag{1}$$

where T is the blackbody temperature of the object or receiver, and the bandwidth of observation depends on the product of the detector intermediate-frequency (IF) bandwidth b and the postdetection bandwidth B of the receiver. Assuming detector and postdetection bandwidths of 5 GHz to match the 200-ps molecular collision time at atmospheric pressure, the estimated thermal noise power at $T_{\rm bb} = 290$ K is $P_{\rm th} = 20$ pW. Mixer noise temperatures are known to increase with frequency ranging from $T_M =$ 400–1000 K over 100–400 GHz (i.e., $T_M \approx 200 + 2\nu_{\rm pr}$ K for probe frequency $\nu_{\rm pr}$ in GHz). If the mixer has a conversion loss of $L_M = 10\log(T_M/T_{\rm bb}) \approx 5$ dB at 358 GHz (i.e., the fraction converted is $f_M = 10^{-L/10} =$ 0.316), only 6 pW of incident thermal noise reaches the IF amplifier. However, the thermal noise is usually dominated by the mixer noise and amplified by the IF amplifier. For a typical IF amplifier with a noise figure $F_N = 1.5$ dB, the effective system temperature $T_s = T_M 10^{F_N/10} = 570$–1400 K and $P_{\rm th} = 39$–97 pW over the 100–400 GHz region [21].

Unlike blackbody, mixer, and amplifier noise, Townes noise arises from a superposition of the electric fields from the received probe and the thermal noise in the waveguide to which the detector is coupled [22]. Consequently, Townes noise power $P_{\rm To} = \sqrt{kT_sBP'_{\rm pr}}$ grows as the square root of the received probe power $P'_{\rm pr}$, and the received SNR is simply

$$\mathrm{SNR} = \sqrt{\frac{P'_{\rm pr}}{kT_sB}}. \tag{2}$$

Figure 2(b) illustrates that for a detector with $B = 5$-GHz bandwidth, Townes noise is the dominant source of noise for scenarios with high received power. For a received probe power of $P'_{\rm pr} = 10$ mW, $P_{\rm To} = 0.62$ μW and SNR = 16 000 at $\nu_{\rm pr} = 100$ GHz, while $P_{\rm To} = 0.88$ μW and SNR = 11 300 at $\nu_{\rm pr} = 300$ GHz because of the higher mixer noise. These SNR values indicate that if the probe beam is pulsed, the "on" state could be discriminated from the "off" state by this SNR. However, DR-based detection uses a continuous-wave probe, and it is the pulsed pump laser that produces the temporal change in the cloud's absorption of the probe that modulates this SNR. For the example above, a pump-induced DR signature that modulates a 10-mW received signal by at least one part in 11 300 to one part in 16 000 per pulse can be detected, depending on $\nu_{\rm pr}$. Moreover, the SNR may be improved as $\sqrt{N}$ by averaging the signal produced by N pump pulses.

III. THz PROPAGATION

The DR signal is also subject to pump-probe beam propagation losses that reduce the SNR. The challenges of THz beam propagation can be separated into three components: diffractive losses associated with the transmitter and retroreflector in a dry lossless atmosphere, atmospheric attenuation, and absorption by the trace-gas cloud, each of which will be considered in turn. A horizontal path is assumed with no obscurations, particulates, hydrometeors, or aerosols in the line of sight that would absorb or scatter the radiation [23,24]. Secondary reactions with other chemicals or water vapor that can alter the composition of the trace cloud are outside the scope of this discussion.

A. Probe propagation in clear atmosphere

We consider a remote sensing methodology that features copropagating pump-probe beams emitted from a colocated transceiver. As shown in Fig. 2(a), the probe beam diffracts away from a $D_{\rm tr} = 1$-m-diameter transceiver dish, interacts with the trace-gas cloud producing the DR signature, and returns to the transceiver from a $D_{\rm rr} = 1$-m-diameter retroreflector up to $R = 1$ km away. To maximize the returned probe SNR, the probe beam is focused on the

retroreflector with a transceiver dish whose focal length $f/\# = R/D_{\rm tr}$. The diffraction-limited Airy disk diameter of the transmitted probe at the retroreflector $d_t = (2.44\lambda_{\rm pr} f/\#)$ may be compared with $D_{\rm rr}$ to ascertain if the probe's optical system is confocal ($d_t < D_{\rm rr}$ or $R < D_{\rm tr}D_{\rm rr}/2.44\lambda_{\rm pr}$), in which case virtually all the probe signal is returned to the transceiver ($f_{\rm tr} = 1$) [25–28]. For $D_{\rm tr} = D_{\rm rr} = 1$ m, the probe system is confocal over an $R = 100$-m range for wavelengths $\lambda_{\rm pr} < 4.1$ mm ($\nu_{\rm pr} > 73$ GHz) and over an $R = 1$-km range for wavelengths $\lambda_{\rm pr} < 0.41$ mm ($\nu_{\rm pr} > 730$ GHz). Chosing the smallest possible $D_{\rm tr}$ and $D_{\rm rr}$ that preserve a confocal geometry provides the largest possible SNR.

For longer wavelengths or longer ranges, the diffracted beam overfills the retroreflector ($d_t > D_{\rm rr}$), so only a fraction $f_t = (D_{\rm tr}D_{\rm rr}/2.44\lambda_{\rm pr}R)^2$ of the transmitted power is reflected. Assuming the probe beam incident on the retroreflector is a plane wave and that the retroreflector has the same $f/\#$ as the transceiver dish, the reflected beam overfills the transceiver antenna by the same fraction, so the fraction of received power is simply

$$f_{\rm tr} = \left(\frac{D_{\rm tr}D_{\rm rr}}{2.44\lambda_{\rm pr}R}\right)^4. \tag{3}$$

Note that the diffractive losses scale as the fourth power of the wavelength, so for a scenario with $R = 1$ km and $D_{\rm tr} = D_{\rm rr} = 1$ m, $f_{\rm tr} = 3.5 \times 10^{-4}$ for $\lambda_{\rm pr} = 3$ mm but grows to $f_{\rm tr} = 2.8 \times 10^{-2}$ at $\lambda_{\rm pr} = 1$ mm. Clearly, DR signatures at short probe wavelengths are desirable.

Diffraction of the IR pump beam is much smaller for the same-sized aperture, so a configuration in which the probe beam is larger than the pump beam [Fig. 2(a)] will ensure that all pump-modulated molecules are interrogated by the probe. For a received probe power of $P'_{\rm pr} = f_{\rm tr}P_{\rm pr}$ for a transmitted probe power $P_{\rm pr}$, Eq. (2) becomes

$$\mathrm{SNR} = \sqrt{\frac{f_{\rm tr}P_{\rm pr}}{kT_sB}}. \tag{4}$$

For $P_{\rm pr} = 10$ mW and $\nu_{\rm pr} = 100$–300 GHz, the SNR is unchanged from 16 000 to 11 300 for the confocal case associated with $R = 100$ m, but for $R = 1$ km, the SNR is reduced to 300 to 1900, respectively. Although the received signal $P'_{\rm pr}$ has dropped by a factor of $f_{\rm tr}$, the SNR has only dropped by $f_{\rm tr}^{1/2}$ at a given frequency because the Townes noise has also decreased.

B. Scenario-dependent atmospheric losses

The millimeter-wave propagation model (MPM) was used to characterize the severity of tropospheric atmospheric attenuation by modeling water-vapor absorption as well as contributions from molecular oxygen, the nonresonant dry-air spectrum, and the water-vapor continuum

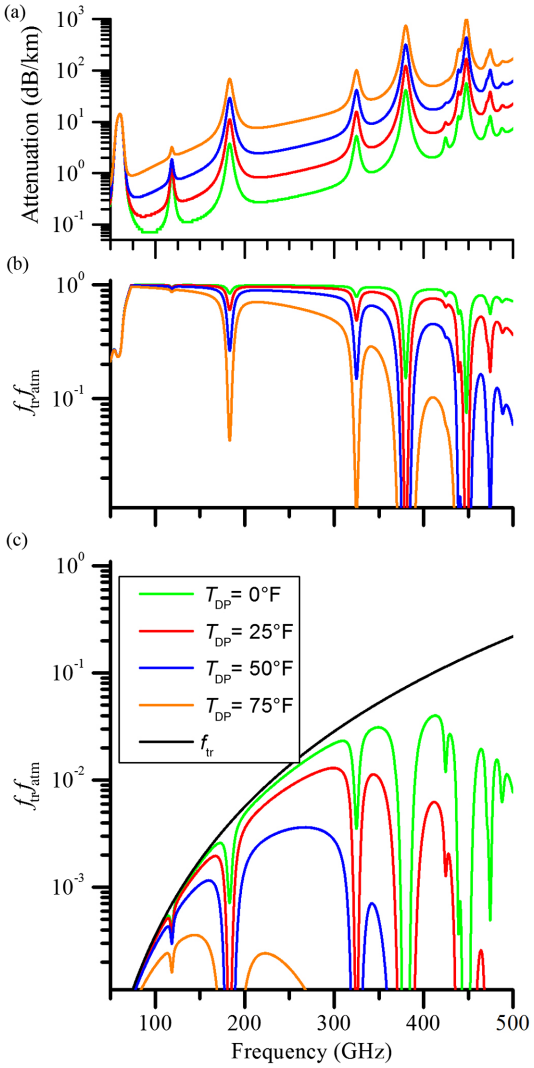

FIG. 3 (a) The atmospheric attenuation as a function of $T_{\rm DP}$ for the frequency region 50–500 GHz, and the fraction of power received at the detector for various $T_{\rm DP}$ at $R = 100$ m (b) and $R = 1$ km (c).

[29,30]. The propagation scenarios considered in this study assume sea-level atmospheric pressure and four dew-point temperatures: $T_{\rm DP} = 0\,^\circ$F (arctic), $25\,^\circ$F (arid), $50\,^\circ$F (temperate), and $75\,^\circ$F (tropical). Atmospheric attenuation is plotted in Fig. 3(a) for the frequency region 50–500 GHz. The fraction of the probe power transmitted through a round-trip path length of $2R$ is $f_{\rm atm} = 10^{-2R\frac{A}{10}}$, where A is the attenuation in dB/km, and R is the single-pass range in kilometers from which the estimated SNR becomes

$$\mathrm{SNR}_{\rm pr} = \sqrt{\frac{f_{\rm atm}f_{\rm tr}P_{\rm pr}}{kT_sB}}. \tag{5}$$

A dew point of $75\,^\circ$F represents the most challenging propagation environment considered. Continuing the

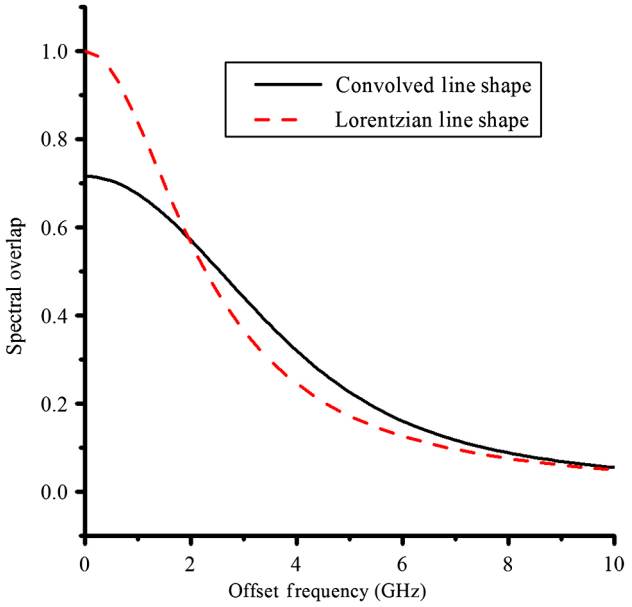

FIG. 4 The convolution $C(\nu_{pu}, \nu_o)$ of the spectral bandwidth of the laser pulse and the pressure-broadened linewidth of a rovibrational transition as a function of pump offset frequency $|\nu_o - \nu_{pu}|$, compared with the Lorentzian line shape $L(\nu, \nu_o)$ appropriate for a cw monochromatic pump.

example from above with $T_{DP} = 75\,°F$, for the $R = 100$ m confocal geometry f_{atm} drops from 0.94 near 100 GHz to 0.25 near 350 GHz [Fig. 3(b)], relatively minor reductions that pose no real limitation on probe frequency. The probe can even be detected at the 183 ($f_{atm} = 0.07$) and 325 GHz (0.01) water lines. However, for the $R = 1$ km scenario, f_{atm} drops from 0.52 near 100 GHz to 10^{-6} near 350 GHz and is even smaller near the water lines, indicating that atmospheric attenuation strongly influences the selection of probe frequency for $T_{DP} = 75\,°F$.

The combination of diffraction and worst-case $T_{DP} = 75\,°F$ atmospheric attenuation thereby constrains the probe window to roughly 90–260 GHz for $R = 1$ km but widens the probe window to 73–500 GHz for $R = 100$ m. The corresponding unmodulated probe SNR values for these scenarios with representative $\nu_{pr} = 100$ and 300 GHz can range from 15 500 and 7900 for $R = 100$ m to 217 and 52 for $R = 1$ km, respectively. For more typical cases, note that atmospheric attenuation decreases rapidly as the dew point drops. Figure 3(c), which plots $f_{tr} f_{atm}$ as a function of ν_{pr} and T_{DP} for $R = 1$ km, shows that diffractive losses dominate atmospheric attenuation even for $T_{DP} = 50\,°F$, suggesting that under most atmospheric conditions, higher-frequency DR signatures ($200 < \nu_{pr} < 300$ GHz) are preferred.

It should be noted that water vapor causes another problem for most THz-based remote sensing methodologies: turbulence-induced attenuation fluctuation and beam wander. However, these millisecond-scale temporal perturbations are frozen on the approximately 200-ps time scale of the IR pulses. Beam wander can cause pulse-to-pulse variation in the pump-probe beams, and very little is known about how an air parcel differentially refracts the pump-probe beams. These temporal fluctuations modify only the degree of overlap between the beams, so the proposed optical system that places the pump beam within the probe beam effectively removes this problem.

IV. DOUBLE-RESONANCE SIGNATURE

Now that the unmodulated probe SNR has been estimated as a function of frequency and dew point, we may estimate the DR spectroscopic signature and detection SNR for an analyte cloud between the transceiver and the retroreflector. The strength of the DR signature depends on many parameters, including the pump-induced change in the probe absorption strength, the column density of the analyte cloud, and the pump intensity. The types of DR spectra and their dependence on the type of rovibrational transition (P, Q, R), the type of vibrational level, and the quantum-mechanical transitional matrix elements are reported elsewhere and will be briefly summarized here [8].

The absorption coefficient for either rovibrational (IR) or rotational (THz) transitions is [31]

$$\alpha = \frac{8\pi^3}{3hc}\nu(n_L - n_U)|\mu|^2 S(\nu, \nu_o) = 3.24 \times 10^{-3}\frac{\nu}{\Delta\nu}(f_L - f_U)\theta|\langle U|\mu_i|L\rangle|^2 m^{-1}, \quad (6)$$

where ν is the frequency of the transition, $n_i = 2.45 \times 10^{13} f_i \theta$ cm^{-3} is the population density of the molecular states connected by the pump ($i = L, U$) for a nondegenerate fractional state population f_i and concentration θ (ppm, at 300 K in an ambient atmosphere of 760 Torr), and $\langle U|\mu_i|L\rangle$ is the appropriate dipole derivative ($\frac{\partial\mu}{\partial Q}$) or dipolar ($\mu$) matrix element for the corresponding rovibrational or rotational transition (Debye). $S(\nu, \nu_o)$ is the line-shape function that simplifies to $1/\pi\Delta\nu$ for peak absorption of a pressure-broadened Lorentzian line shape, with $\Delta\nu_{THz} = \Delta\nu_{IR} \approx 2.3$ GHz HWHM assuming a pressure-broadening parameter of 3 MHz/Torr [32]. For a trace gas, the absorption of the probe by the cloud (α_{pr}) slightly reduces the received probe power P'_{pr} or SNR_{pr}, while the IR absorption by the cloud is the means by which the pump laser excites the cloud. Indeed, the laser-pulse width should match the FWHM of the IR transition: $1/4.6$ GHz ≈ 200 ps.

A. Pump rate

Equation (6) may be used to calculate the DR signal strength induced by the IR pump at ν_{pu}. The ability of the pump to drive the rovibrational transition at ν_o depends on the spectral overlap of the two, which may be calculated as

a convolution $C(\nu_{pu},\nu_o)$ of the spectral bandwidth of the area-normalized Gaussian $G(\nu,\nu_{pu})$ laser pulse with the pressure-broadened amplitude-normalized Lorentzian $L(\nu,\nu_o)$ line shape of the IR transition. Because the optimal strategy would ordinarily adjust the pump-beam diameter so that the Rabi broadening is less than or equal to the pressure broadening, we will not include these effects here. Figure 4 compares $C(\nu_{pu},\nu_o)$ with the Lorentzian line-shape efficiency—to which $C(\nu_{pu},\nu_o)$ converges for a cw monochromatic pump—and indicates that the pulsed pump is slightly less efficient at line center ($\nu_{pu}=\nu_o$) but more efficient for pump frequencies more than $\Delta\nu_{IR}$ away from line center. This is critically important because DR transitions having a pump offset $|\nu_o-\nu_{pu}|$ as large as $5\Delta\nu_{IR}$ may still produce strong DR signals, perhaps even producing the optimum choice for the highest SNR in a given scenario. For example, the CH_3F coincidences have $|\nu_o-\nu_{pu}|$ that range from 1.59 to 10.1 GHz, and the strongest SNR occurs for $9P(22)$ which has $\nu_o-\nu_{pu}=4.82$ GHz.

When the spectral profile of a transform-limited $\tau_{pu}=200$-ps pump laser pulse (FWHM spectral bandwidth $\Delta\nu_{pu}=5$ GHz) is convolved with the amplitude-normalized $\Delta\nu_{IR}=2.3$ GHz HWHM pressure-broadened transition, the spectral overlap line-shape function $C(\nu_{pu},\nu_o)$ shown in Fig. 4 indicates a rovibrational transition may be excited within approximately 10 GHz of the center frequency. Using this, the rate (s^{-1}) at which molecules are pumped per laser pulse is

$$R_{pump}=\frac{\alpha_{IR}\varepsilon}{(\pi r_{pu}^2)(h\nu_{pu})(\tau_{pu}n_L)}=\frac{32\pi^2}{3h^2c}\frac{\varepsilon}{D_{pu}^2\tau_{pu}}\left|\langle U|\frac{\partial\mu}{\partial Q}|L\rangle\right|^2 C(\nu_{pu},\nu_o), \quad (7)$$

where ε is the laser pump energy per pulse. Note that the pump beam should never be larger than the received probe beam ($D_{pu}\le D_{tr}$) to ensure all molecules pumped are probed.

B. Modulated absorption

The DR signature is the pump-induced change in absorption coefficient ($\Delta\alpha$) given by [8]

$$\Delta\alpha=\pm\frac{32\pi}{3h^2c}\left[\left|\langle U|\mu|L\rangle\right|^2\frac{\nu_{THz}}{\Delta\nu_{THz}}\right]\left[\frac{\alpha_{IR}}{\nu_{pu}D_{pu}^2}\varepsilon\right], \quad (8)$$

where ν_{THz} (usually $=\nu_{pr}$) corresponds to the monitored transition with the indicated transition matrix element. Assuming no pump saturation and minimal Rabi broadening, the DR absorption strengths $\Delta\alpha$ (m^{-1}) grow linearly with IR pump pulse energy ε and concentration θ (via α_{IR}).

The DR spectral signature associated with this pump-induced $\Delta\alpha$ is rich, complex, and unique for each molecular isotopomer. As noted above, four DR signatures are produced for each rovibrational transition excited by a pump coincidence, two exhibiting positive ($+\Delta\alpha$) and two exhibiting negative ($-\Delta\alpha$) changes in absorption, one each in the ground and excited vibrational levels. Another reason higher frequencies are preferred for DR spectroscopy for all but the highest dew points is that $\Delta\alpha$ grows linearly with rotational frequency ν_{THz}. The strength of $\Delta\alpha$ for an individual transition may also be affected by nearby rovibrational transitions simultaneously pumped by the laser. The cumulative effect of these overlapping transitions strengthens or weakens the total $\sum[\Delta\alpha_i(\nu_{pr})]=\Delta\alpha_i(\nu_{pr})\prod(\nu_{pr})$ at ν_{pr} as compared to the $\Delta\alpha_i(\nu_{pr})$ of the constituent transitions by a transition-specific overlap parameter $\prod(\nu_{pr})$ [8].

C. Differential SNR

The differential SNR of each pump-induced DR signature may now be estimated for a cloud of length l assuming the pump beam is entirely within the probe beam. Disregarding diffraction and atmospheric attenuation for the moment, the pump-induced modulation in transmitted probe power ΔP_{pr} for a single isolated transition is

$$\begin{aligned}\Delta P_{pr}&=P_{pr}(\text{pump off})-P_{pr}(\text{pump on})\\&=P_{pr}e^{-2\alpha_{THz}l}-P_{pr}e^{-(\Delta\alpha+2\alpha_{THz})l}\\&\approx P_{pr}(1-e^{-\Delta\alpha l})\approx P_{pr}\Delta\alpha l,\end{aligned} \quad (9)$$

where the final approximations apply to the common case in which $2\alpha_{pr}l<\Delta\alpha l<1$, especially when probing a DR signature from a transition in the excited vibrational level. Including all attenuation and noise factors, the integrated SNR for the DR technique is simply

$$SNR_{DR}=(\Delta\alpha f_i\theta l)SNR_{pr}, \quad (10)$$

where θ is the concentration of the trace cloud, usually given in parts per million, f_i is the isotopic abundance, and $\Delta\alpha$ was calculated for parts-per-million (ppm) concentrations. Unless the pump intensity is so high that the IR transition is saturated, the SNR_{DR} grows linearly with laser pulse energy and total path concentration of the cloud θl (ppm m) but only as the square root of the probe power because of Townes noise. Therefore, it is more effective to increase the SNR by increasing pulse energy ε than by increasing the probe power P_{pr}, an important technological consideration. Note that the amount of Townes noise is insignificantly altered by the DR modulation of the probe for the common scenario $\Delta\alpha l\ll 1$.

The SNR_{DR} may be factored into terms that depend only on molecular parameters and terms that depend on the scenario. We define $\Delta\alpha^{\dagger}$ [$(J/m^2)^{-1}$ $(\text{ppm m})^{-1}$] as the product of those terms that depend only on molecular parameters,

$$\Delta\alpha^{\dagger} = \Delta\alpha \prod(\nu_{\mathrm{pr}}) \left(\frac{D_{\mathrm{pu}}^2}{\varepsilon}\right) = \pm \frac{32\pi}{3h^2 c} \left[|\langle U|\mu|L\rangle|^2 \frac{\nu_{\mathrm{THz}}}{\Delta\nu_{\mathrm{THz}}}\right] \left[\frac{\alpha_{\mathrm{IR}} \prod(\nu_{\mathrm{pr}})}{\nu_{\mathrm{pu}}}\right], \quad (11)$$

where the factor $\Pi(\nu_{\mathrm{pr}})$ captures the contribution of overlapping transitions at ν_{pr}. Tables of $\Delta\alpha^{\dagger}$ may be deduced from measurements of any molecule or tabulated from $\Delta\alpha$ following the methodology outlined in Ref. [8] for a 100 ppm m cloud and a cw pump with $D_{\mathrm{pu}} = 1$ m. The scenario-dependent parameters in brackets

$$\mathrm{SNR}_{\mathrm{DR}} = \Delta\alpha^{\dagger} \left[\left(\frac{\varepsilon}{D_{\mathrm{pu}}^2}\right)(f_i \theta l)\mathrm{SNR}_{\mathrm{pr}}\sqrt{N}\right] = \Delta\alpha^{\dagger} \left(\frac{\varepsilon(f_i \theta l)}{D_{\mathrm{pu}}^2}\right)\sqrt{\frac{N P_{\mathrm{pr}} f_{\mathrm{atm}} f_{\mathrm{tr}}}{k T_s B}} \quad (12)$$

include the pump energy per pulse ε and radius D_{pu}, the θl concentration, and the probe $\mathrm{SNR}_{\mathrm{pr}}$ from Eq. (5). The $\sqrt{N}$ term represents the improved SNR achieved by signal averaging N pump pulses.

V. TRANSITION SELECTION: AN EXAMPLE USING CH_3F

This methodology may be used to identify the scenario-dependent molecule-specific combination of pump-probe frequency DR signatures. The methodology will first be applied to the analysis of CH_3F to illustrate how the optimal signatures may be selected, then additional complexity will be addressed by considering the principal isotopomers of CH_3Cl and CH_3Br. These molecules are chosen as prototypical because their spectra is well characterized and may be modeled analytically, while their corresponding DR signatures are dramatically different and illustrate characteristics that may be generalized [8]. To begin the discussion of scenario-dependent detection $\mathrm{SNR}_{\mathrm{DR}}$ (hereafter called simply "SNR"), the analysis of DR signatures below 500 GHz will consider $\theta l = 100$ ppm m for two cases: a "standard" (S) 100-m range with $T_{\mathrm{DP}} = 50\,^{\circ}\mathrm{F}$, $P_{\mathrm{pr}} = 10$ mW, $\varepsilon = 10$ mJ/pulse, and $D_{\mathrm{pu}} = 10$ cm, and a "long-range tropical" (LRT) 1-km range with $T_{\mathrm{DP}} = 75\,^{\circ}\mathrm{F}$, $P_{\mathrm{pr}} = 1$ W, $\varepsilon = 1$ J/pulse, and $D_{\mathrm{pu}} = 1$ m. Because of atmospheric attenuation and diffraction of the probe beam in the LRT scenario, the probe power, pump energy, and pump cross-sectional area are all increased 100 times.

Table I and Figs. 5(a)–5(c) present and compare $\Delta\alpha^{\dagger}$ spectra and scenario-dependent SNR values for each DR

TABLE I. Double-resonance $\Delta\alpha^{\dagger}$ and SNR estimates assuming baseline parameters for two scenarios: a standard (S) 100-m range and a long-range tropical (LRT) 1-km range. The subscript notation $0{:}n$ indicates pump excitation of all rovibrational transitions with $K = 0 - n$.

Laser line	Transition	$\nu_o - \nu_{\mathrm{pu}}$ (GHz)	ν_{pr} (GHz) $\Delta\alpha^{\dagger}[(\mathrm{J/m^2})^{-1}\ (\mathrm{ppm\,m})^{-1}]$ SNR (S, LRT)			
$9P(22)$	$P_{0:1}(2)$	4.82	102	153	50.4	101
			19.1×10^{-6}	-15.9×10^{-6}	-5.28×10^{-6}	19.1×10^{-6}
			303, 43.1	218, 41.1	45.9, 3.98	310, 43
$9P(24)$	$P_{0:2}(3)$	8.07	153	204	101	151
			15.8×10^{-6}	-13.8×10^{-6}	-6.01×10^{-6}	15.8×10^{-6}
			225, 42.4	167, 21.6	94.1, 13	212, 40.5
$9P(20)$	$P_0(1)$	1.59	51.1	102		50.4
			13.2×10^{-6}	-9.23×10^{-6}	…	13.2×10^{-6}
			118, 9.97	145, 20.4		115, 9.96
$9P(12)$	$R_{0:2}(2)$	−10.1	102	153	151	202
			3.89×10^{-6}	-9.69×10^{-6}	-9.25×10^{-6}	8.83×10^{-6}
			61.1, 8.57	138, 25.9	125, 23.7	104, 12.3
$9P(18)$	$Q_{0:3}(3)$	−5.57	153	204	151	202
			-5.61×10^{-6}	-12.2×10^{-6}	5.31×10^{-6}	11.7×10^{-6}
			67.5, 12.7	135, 17.4	80.2, 15.3	111, 13.1
$9P(18)$	$Q_{0:4}(4)$	−8.27	204	255	202	252
			-12.2×10^{-6}	-10.5×10^{-6}	11.7×10^{-6}	10.1×10^{-6}
			135, 17.4	108, 14.5	111, 13.1	112, 15.5
$9P(14)$	$R_{0:1}(1)$	−7.36	51.1	102	101	151
			2.34×10^{-6}	-7.17×10^{-6}	-6.70×10^{-6}	6.94×10^{-6}
			20.8, 1.77	115, 16.1	110, 15.3	95.9, 18.3

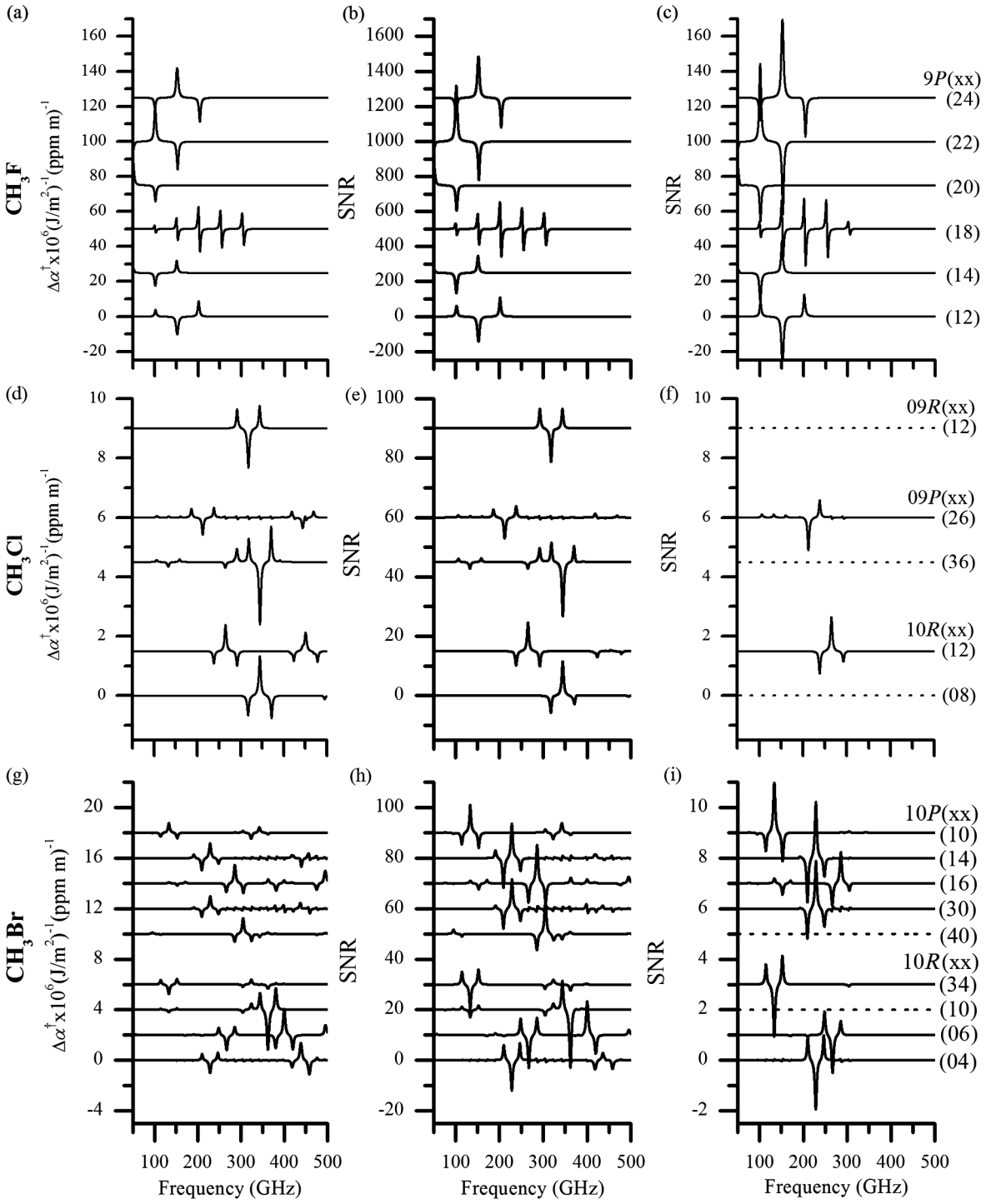

FIG. 5 IR-THz DR transition strength $\Delta\alpha^{\dagger}$ (a),(d),(g) for the standard case and the SNR for the standard (b),(e),(h) and long-range tropical (c),(f),(i) scenarios for CH_3F (a)–(c), CH_3Cl (d)–(f), and CH_3Br (g)–(i). Each laser line labeled at the right is coincident with a transition that produces a SNR ≥ 1 for a 100–ppm m cloud.

transition produced by the frequency coincidence of a line from a CO_2 pump laser and a specific CH_3F rovibrational transition. First, examining the $\Delta\alpha^{\dagger}$ spectra for the six pump coincidences that produce DR signatures below 500 GHz, the basic P- ($\Delta J = -1$), Q- ($\Delta J = 0$), and R-branch ($\Delta J = +1$) behaviors become clear. For P- [i.e., $9P(20)$, $9P(22)$, and $9P(24)$] and R-branch transitions [i.e., $9P(12)$ and $9P(14)$], a triplet of features is observed, two of which are separated by twice the principal rotational constant B_0, between which an overlapping doublet forms a central peak of opposite polarity. The Q-branch DR signatures from the $9P(18)$ line are

fundamentally different in behavior because multiple $\Delta J = 0$ transitions are simultaneously excited, each one of which represents a nearly overlapping doublet whose components have opposite polarity.

These $\Delta\alpha^{\dagger}$ spectra are then modified by the effects of diffraction and atmospheric attenuation to estimate the SNR using Eq. (12). The DR spectra for the standard scenario remain almost unchanged by these effects, and the SNR exceeds 100 for several transitions assuming the "baseline parameters" of $N = 100\,\text{pulses/sec}$, $D_{\text{tr}} = D_{\text{rr}} = 1$ m, and $\theta l = 100$ ppm m for 1 s of acquisition time. The strongest features are the overlapping doublets of the P-branch transitions near 101 and 102 GHz (SNR approximately 310 and 303, respectively). The SNR for alternative scenarios may be obtained by scaling these standard-scenario SNR values by $\varepsilon\sqrt{P_{\text{pr}}}D_{\text{pu}}^{-2}$. From this, we may estimate the standard- scenario detection threshold (SNR = 1) for baseline parameters with a probe beam at 102 GHz to be $\varepsilon^{T} = 33\ \mu\text{J/pulse}$ for $P_{\text{pr}} = 10$ mW or $P_{\text{pr}}^{T} = 100$ nW for $\varepsilon = 10$ mJ/pulse. A plot of detection threshold as a function of ε and P_{pr} for four concentrations of CH_3F is presented in Fig. 6(a). The DR spectra for the LRT scenario are much weaker for the baseline parameters, especially at the highest frequencies where atmospheric attenuation is most severe. The SNR for most transitions is < 20, and the same P-branch transitions produce the strongest DR signals (SNR = 40–43).

For pump-probe powers above this detection threshold, the minimum detectable cloud concentration may be estimated. Using the baseline parameters above, assuming a common probe frequency of 102 GHz for both scenarios, the concentration detection threshold is $100\ \text{ppm m}/303 = 330\ \text{ppb m}$ for the standard scenario and $100\ \text{ppm m}/43.1 = 2.3\ \text{ppm m}$ for the long-range tropical scenario. The minimum detectable concentration $(\theta l)_{\text{min}}$ may be estimated by recognizing that a coherent π pump pulse will swap population densities $n_U \leftrightarrow n_L$. The strongest-possible $\Delta\alpha$ is induced by a π pump pulse, producing $\Delta\alpha_{\text{max}} = \alpha_{\text{pr}}\frac{kT}{h\nu_{\text{pr}}}$, effectively removing the requirement to calculate the $\Delta\alpha$ signatures for isolated transitions. Although the pump intensity required for a 200 ps pulse to produce this π pulse may be easily calculated using standard Rabi formalism, it is only necessary to insert $\Delta\alpha_{\text{max}}$ into Eq. (10) to estimate the maximum possible SNR_{DR} following such a π pulse. In addition, if we set $\text{SNR}_{\text{DR}} = 1$, the minimum detectable concentration

$$(\theta l)_{\text{min}} = \left[\prod \alpha_{\text{pr}}\frac{kT}{h\nu_{\text{pr}}} f_i \text{SNR}_{\text{pr}}\sqrt{N}\right]^{-1} \qquad (13)$$

may be easily estimated for any scenario. This equation leads to a critical insight: all factors except the frequency-dependent Π may be calculated solely by examination of the probe transitions. For the standard and LRT scenarios, $(\theta l)_{\text{min}} = 71$ and 505 ppb m, respectively.

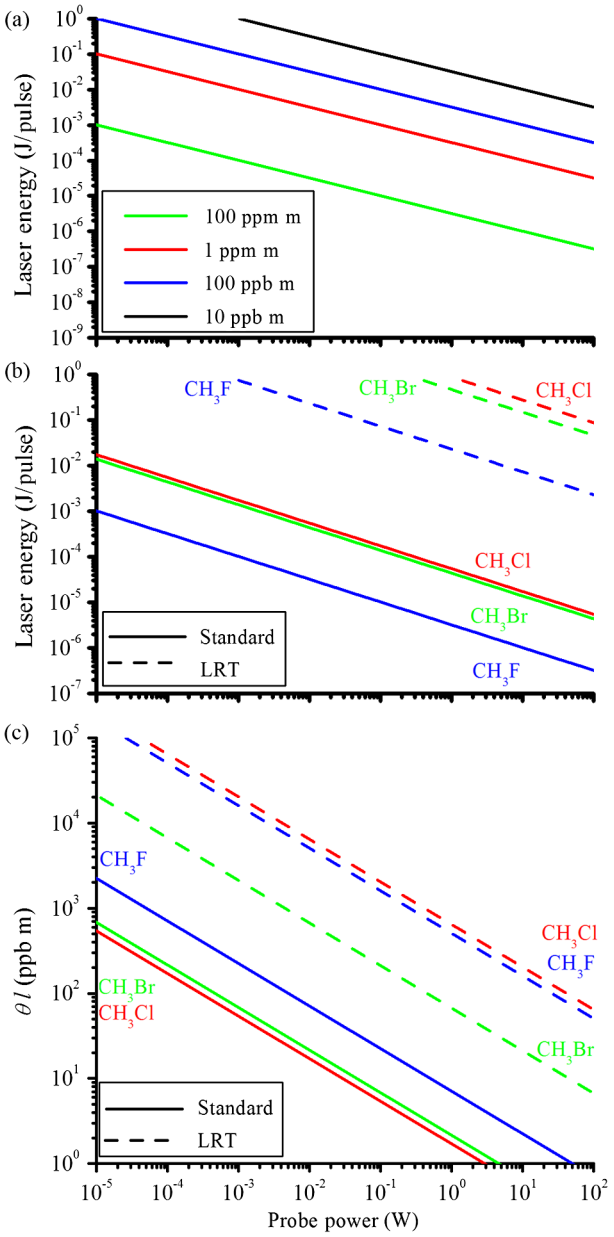

FIG. 6 (a) Detection-threshold pump energy per pulse as a function of probe power for various concentrations of CH_3F with the standard scenario. (b) Scenario-dependent detection thresholds for a 100–ppm m cloud of CH_3F, CH_3Cl, and CH_3Br. Laser lines and probe frequencies used for analysis correspond to the strongest SNR given for each molecule in Tables I–III. (c) Scenario-dependent minimum detection threshold for π-pulse excitation of CH_3F, CH_3Cl, and CH_3Br.

VI. DR SPECTRAL ANALYSIS FOR METHYL HALIDES

The analysis is expanded to consider two additional methyl halide molecules, CH_3Cl and CH_3Br, which are

TABLE II. Double-resonance $\Delta\alpha^{\dagger}$ signature and SNR calculations of $CH_3{}^{35}Cl$ ($f_i = 0.76$) assuming baseline parameters for two scenarios: a standard 100-m range and a long-range tropical 1-km range. Transitions listed represent the strongest SNRs for each scenario.

Laser line	Transition	$\nu_o - \nu_{pu}$ (GHz)	ν_{pr} (GHz)	$\Delta\alpha^{\dagger}$ $[(J/m^2)^{-1}\ (ppm\,m)^{-1}]$	SNR (Standard)	SNR (LRT)
$9P(36)$	${}^{R}R_0(12)$	−0.308	345	-2.0×10^{-6}	18.2	···
$10R(08)$	${}^{P}P_6(13)$	0.765	345	1.25×10^{-6}	11.3	···
$9R(12)$	${}^{R}R_6(11)$, ${}^{R}P_9(13)$	−0.032, −5.84	318	-1.25×10^{-6}	11.2	···
$10R(12)$	${}^{P}P_6(10)$	−1.5	265	0.852×10^{-6}	9.61	1.14
$9P(26)$	${}^{R}P_4(8)$, ${}^{R}R_3(7)$, ${}^{R}Q_3(7)$, ${}^{R}Q_3(8)$	0.685, −1.28, −0.663, −1.44	212	-0.569×10^{-6}	6.98	1.10

structurally similar to CH_3F but produce quite different DR signatures. The CO_2 pump laser is coincident with rovibrational transitions involving the V_6 bending mode whose dipole derivative, absorption coefficient α_{IR}, and pump rate are much smaller than in the V_3 stretching mode in CH_3F [8]. The bending motion of the V_6 mode also couples to the molecular rotation, generating *l*-doubled rotational transitions that produce significantly more rovibrational transitions coincident with pump laser lines and a much more complex DR spectrum. Indeed, a single laser line may simultaneously pump *P*-, *Q*-, and *R*-branch transitions, producing DR signatures characterized by overlapping *P*-, *Q*-, and *R*-branch forms, as illustrated in Figs. 5(d)–5(f) for the CH_3Cl DR spectra excited by the $9P(26)$ and $9P(36)$ laser lines. Finally, both CH_3Cl and CH_3Br have naturally abundant isotopic isomers with rotational spectra that are similar but easily discriminated from the primary isotopomer.

Tables II and III and corresponding Figs. 5(d)–5(i) identify some of the strongest DR signatures with the highest $\Delta\alpha^{\dagger}$ values for the two most abundant isotopomers of CH_3Cl and CH_3Br. Values of the SNR for the standard and LRT scenarios are plotted and presented using the baseline parameters discussed in Sec. IV. The SNR for varying pump-probe powers, the detection threshold powers, and the minimal detectable concentrations may be estimated following the procedures outlined in the previous section.

Examination of Tables II and III also reveals that the optimal pump-probe transitions for CH_3Cl and CH_3Br are scenario dependent. While some slight advantage can be gained by changing the probe frequency in CH_3F between scenarios, the pump transition is unchanged for the two cases examined. This is primarily the result of the relative sparsity of coincidences in CH_3F whose DR transitions occur at frequencies where diffraction and atmospheric attenuation are minimal.

Comparing the amplitudes of the spectra in Figs 5(d)–5(i) with Figs. 5(a)–5(c) illustrates the reduced strength of the IR transition matrix elements for bending vs stretching modes. For the LRT scenario using the baseline pump energy (1 J) and probe power (1 W), the minimum column density required for detecting CH_3F is only $\theta l = 2.3$ ppm m, whereas 88 and 47 ppm m are required to detect CH_3Cl and CH_3Br, respectively.

TABLE III. Double-resonance $\Delta\alpha^{\dagger}$ signature and SNR calculations of CH_3Br assuming baseline parameters for two scenarios: a standard 100-m range and a long-range tropical 1-km range. Transitions listed represent the strongest SNRs for each scenario. All transitions have contributions from both $CH_3{}^{79}Br$ and $CH_3{}^{81}Br$.

Laser line	Transition	$\nu_o - \nu_{pu}$ (GHz)	ν_{pr} (GHz)	$\Delta\alpha^{\dagger}$ $[(J/m^2)^{-1}\ (ppm\,m)^{-1}]$	SNR (Standard)	SNR (LRT)
$10R(10)$	${}^{R}R_0(18)$	−0.199	362	-2.05×10^{-6}	22.9	···
$10P(16)$	${}^{R}P_0(15)$	−3.16	286	0.817×10^{-6}	15.1	1.23
$10R(06)$	${}^{R}P_3(21)$	0.117	400	1.06×10^{-6}	13.3	1.50
$10R(06)$	${}^{R}R_0(13)$	−3.32	267	-0.861×10^{-6}	13.0	···
$10P(14)$	${}^{R}P_0(12)$, ${}^{P}Q_1(12)$, ${}^{P}Q_1(11)$, ${}^{P}R_2(10)$	3.83,[a] 8.60,[a] 9.41,[a] 0.616[a]	229	0.615×10^{-6}	13.2	2.15
$10P(40)$	${}^{P}P_3(16)$	−4.06	305	0.740×10^{-6}	12.4	···
$10R(04)$	${}^{R}P_2(12)$, ${}^{R}Q_1(12)$, ${}^{R}Q_1(11)$, ${}^{R}R_0(11)$	−2.16, −0.037, −0.779, 2.03[a]	228	-0.775×10^{-6}	11.5	1.88
$10P(30)$	${}^{P}P_2(12)$, ${}^{P}Q_3(12)$, ${}^{P}Q_3(11)$, ${}^{P}R_4(10)$	−2.13, 7.38, 8.19, 1.31	229	0.565×10^{-6}	11.5	1.87
$10R(34)$	${}^{R}R_3(06)$	2.25[a]	133	-0.486×10^{-6}	10.8	2.01
$10P(10)$	${}^{R}P_0(07)$	0.168[a]	133	0.393×10^{-6}	10.6	1.97

[a]Laser offset reported is for $CH_3{}^{81}Br$, which is less than the laser offset for $CH_3{}^{79}Br$.

It should be noted that the DR transitions identified in the tables are reported for a specific probe frequency corresponding to a specific rotational transition. In some cases, the contribution from overlapping rovibrational transitions produces a DR spectrum that may have an even higher SNR at a frequency slightly offset from a listed rotational transition. For example, the SNR from the $9P(26)$ CO_2 laser line in CH_3Cl is coincident with several rovibrational transitions that produce DR signatures. The reported probe frequency in Table II is a rotational transition excited by the ${}^RR_3(7)$ rovibrational transition with SNR = 6.98; however, the ${}^RQ_3(7)$, ${}^RQ_3(8)$, and ${}^RP_4(8)$ transitions also contribute to the SNR at 212 GHz, and the peak SNR = 7.04 occurs at 212.2 GHz.

A. Methyl chloride

For CH_3Cl, there are two common isotopomers: ${}^{12}CH_3{}^{35}Cl$ ($f_i = 0.76$) and ${}^{12}CH_3{}^{37}Cl$ ($f_i = 0.24$). For DR signatures below 500 GHz, all 68 CO_2 laser lines considered produced rovibrational coincidences, a total of 942 for ${}^{12}CH_3{}^{35}Cl$ and 955 for ${}^{12}CH_3{}^{37}Cl$. The strongest lines for the standard and LRT scenario are summarized in Table II, and Figs. 5(d)–5(f) compare the $\Delta\alpha^\dagger$ spectra and the scenario-dependent SNR. While both isotopic variants are considered in this analysis, ${}^{12}CH_3{}^{35}Cl$ is responsible for all of the strongest transitions listed in Table II.

The overlapping R-branch doublet near 345 GHz pumped by the $9P(36)$ laser line produces the strongest $SNR_{DR} = 18.2$ for the baseline parameters in the standard scenario. The detection threshold (SNR = 1) for a 100–ppm m cloud in the standard scenario is thereby estimated to be $\varepsilon^T = 550$ μJ/pulse for $P_{pr} = 10$ mW or $P_{pr}^T = 30$ μW for $\varepsilon = 10$ mJ/pulse. A plot of detection threshold as a function of ε and P_{pr} for the standard and LRT scenarios is presented in Fig. 6(b). The concentration detection threshold for the standard scenario is $\theta l = 5.5$ ppm m.

In the LRT scenario, atmospheric attenuation prevents almost all DR signatures from being measured. Indeed, only two transitions produce a SNR ≥ 1 using baseline parameters: the ${}^PP_6(10)$ transition excited by the $10R(12)$ laser line with a probe frequency of 265 GHz, and several rovibrational transitions excited by the $9P(26)$ laser line with a probe frequency of 212 GHz [Figs. 5(d)–5(f)]. CH_3Cl represents a worst case in the LRT scenario because of its weak infrared absorption coefficient, l-doubled transitions, and spectrally resolved isotopomers. However, its minimum detectable concentrations, given a π pump pulse, are $(\theta l)_{min} = 17$ and 640 ppb m for the respective standard and LRT scenarios, comparable to the CH_3F detection limits. It is only because the pump is more weakly absorbed by CH_3Cl than CH_3F that the SNRs are smaller.

B. Methyl bromide

Methyl bromide has two common isotopomers of nearly equal abundance: ${}^{12}CH_3{}^{79}Br$ ($f_i = 0.51$) and ${}^{12}CH_3{}^{81}Br$ ($f_i = 0.49$). The isotopic difference in V_6 vibrational energy is much smaller in CH_3Br than in CH_3Cl, so many laser coincidences are shared between the two isotopes and produce similar often overlapping DR signatures. Indeed, all of the strongest DR signatures (Table III) are doubled in strength because of this isotopic spectral overlap. All 68 CO_2 laser lines considered produced coincidences, a total of 1779 for the two primary isotopes in CH_3Br. As compared to CH_3Cl, CH_3Br is more easily detected because the larger mass of CH_3Br produces a greater blending of the P-, Q-, and R-branch transitions, shifts the strongest $\Delta\alpha^\dagger$ signatures to lower frequencies, and generates a more richly overlapping DR spectrum [Fig. 5(g)].

For the standard scenario, $10R(10)$ excites the ${}^RR_0(18)$ transition of both isotopes and generates overlapping DR spectra which combine to produce the strongest $SNR_{DR} = 22.9$ at 362 GHz [Figs. 5(g)–5(i)]. For a 100–ppm m cloud and corresponding baseline parameters with $P_{pr} = 10$ mW, the detection threshold pump energy $\varepsilon^T = 440$ μJ/pulse, and the threshold pump power $P_{pr}^T = 19$ μW for $\varepsilon = 10$ mJ/pulse. The minimum concentration required for detection using baseline parameters is $\theta l = 4.4$ ppm m.

For the LRT scenario, CH_3Br has multiple coincidences produce a SNR > 1, the strongest of which ($SNR_{DR} \approx 2$) are located at 229 and 133 GHz excited by the $10P(14)$ and $10R(34)$ laser lines, respectively. Note that the heavier CH_3Br has more DR signatures in the low-frequency atmospheric windows than the lighter CH_3F and CH_3Cl, suggesting that even heavier molecules will have even more detectable coincidences.

Note also that the minimum detectable concentration $(\theta l)_{min}$ assuming π pump pulse for CH_3Br is between those for CH_3F and CH_3Cl for the standard case, but is much lower for the LRT scenario because the probe frequency resides within an atmospheric transmission window.

C. Specificity

The power of this technique derives from its unprecedented recognition specificity for atmospheric remote sensing achieved by the rare coincidence of pump laser lines with molecular rovibrational transitions and the uniqueness of the resulting DR signature. The two spectral dimensions of recognition—IR pump and THz probe—suggest a two-dimensional specificity matrix may be constructed for molecular identification. Figure 5 constitutes the scenario-dependent specificity matrix for CH_3F, CH_3Cl, and CH_3Br, respectively. The P-, Q-, and R-dependent DR spectral shapes and associated $\Delta\alpha^\dagger$ polarity differences represent an additional degree of recognition specificity. It is clear that by appropriately selecting a laser line and probing at a specific frequency, these three

molecules can be separately identified in a mixture up to 1 km away.

Ideally, one will simply choose the strongest DR signature for a given molecule to detect and recognize it, and that will work for all the transitions presented in Tables I–III. However, these tables do not include all of the coincidences of CH_3Cl and CH_3Br, and it is common that a given laser line can pump listed or unlisted transitions in more than one molecule. The pressure-broadened Lorentzian tails of these DR signatures extend very far from the peaks, dropping to 10% and 2% of the peak value three and seven linewidths away, respectively. For example, in the standard scenario, the strongest feature of CH_3F will still have $SNR_{DR} > 7.1$ up to $7\Delta\nu_{THz} \approx 16$ GHz away, while it is undetectable at $SNR_{DR} = 0.88$ in the LRT scenario. These long tails can produce a possible false positive identification of a molecule that shares a pump laser line with CH_3F but whose probe may be offset by a significant amount. Note that the probability of false positive detection (PFPD) depends strongly on atmospheric

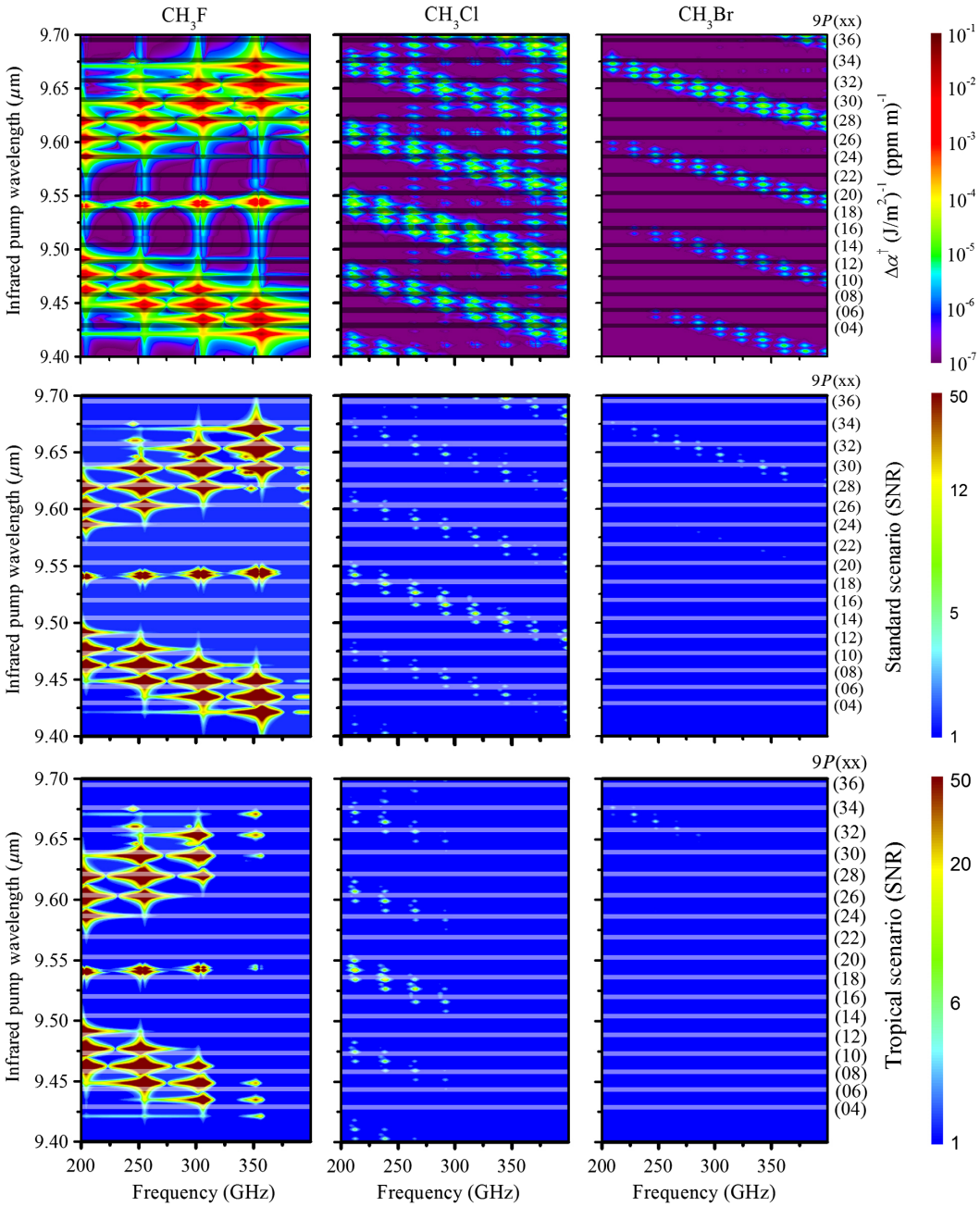

FIG. 7 (Top row) Plots of $|\Delta\alpha^{\dagger}|$ as a function of pump wavelength and probe frequency for CH_3F, CH_3Cl, and CH_3Br. (Center row) Similar plots of SNR for the standard scenario. (Bottom row) Similar plots of SNR for the LRT scenario. Values for SNR < 1 are not plotted.

conditions; the PFPD is actually lowest in the "unfavorable" LRT scenario which most strongly attenuates these tails.

This is illustrated in Fig. 7, where the process for quantitatively estimating recognition specificity and PFPD is outlined using a portion of the specificity matrix. The top row of figures plots $|\Delta\alpha^{\dagger}|$ for each molecule, including all isotopomers with their natural abundances, for the 9.4–9.7 μm, 200–400 GHz portion of the specificity matrix, overlaid by the $9P(xx)$ CO_2 laser lines. These plots illustrate the extent of the long Lorentzian tails over THz probe frequencies and IR pump wavelengths. Notice that the tails for CH_3F are often much stronger than the strongest features for CH_3Cl or CH_3Br, hence the concern that trace amounts of CH_3F can produce a nontrivial PFPD when trying to detect CH_3Cl or CH_3Br. Not only do these long tails produce DR signatures at THz probe frequencies far from the coincidence, they also allow the IR pump lines adjacent to a coincident pump line to produce a DR signature.

However, this problem is not as severe as it appears in realistic scenarios. The center and bottom rows in Fig. 7 illustrate how atmospheric attenuation in the respective standard and LRT scenarios significantly reduces the PFPD by driving the SNR of these tails below 1. These specificity matrix plots clearly show that the optimal DR signature for recognizing a given trace gas is not necessarily the strongest DR signature but the strongest one that does not overlap with obscuring features from other trace gases.

One way to quantify this is to calculate the PFPD or, equivalently, the interferent gas concentration required to produce a DR signature as strong as the DR signature from the gas being interrogated. Specifically, Eq. (12) may be used to calculate the concentration $(\theta l)_j$ required of molecule j to produce a false positive detection (i.e., a DR SNR of equal strength) when attempting to discriminate molecule i with concentration $(\theta l)_i$. Two aspects of Eq. (12) simplify and generalize this calculation: for a given pump line and probe frequency, the SNR depends linearly on θl, and the interferent and the target gases are equally affected by the scenario. Consequently, the condition $\mathrm{SNR}_i = \mathrm{SNR}_j$ reduces to $\Delta\alpha_i^{\dagger}(\theta l)_i = \Delta\alpha_j^{\dagger}(\theta l)_j$ for all scenarios, from which we may define $\Xi_j(i) = \Delta\alpha_i^{\dagger}/\Delta\alpha_j^{\dagger}$ when $(\theta l)_i = (\theta l)_j$. It is easy to see that $\Xi_j(i)^{-1}$ is the probability of falsely identifying interferent j instead of an equal concentration of target i. It follows that concentration $(\theta l)_j \geq \Xi_j(i)(\theta l)_i$ is required to produce a larger SNR from interferent j than from target i. Since the $\mathrm{PFPD} = \Xi_j(i)^{-1}$, locations within the specificity matrix that produce $\Xi_j(i) \gg 1$ are most favored for discriminating target i from interferent j. Therefore, the pump line and probe frequency best suited for recognizing an analyte is the one that produces the largest value of $\Xi_{\min}(i) = \Delta\alpha_i^{\dagger}/\max(\Delta\alpha_{j\neq i}^{\dagger})$ for all gases represented in the matrix.

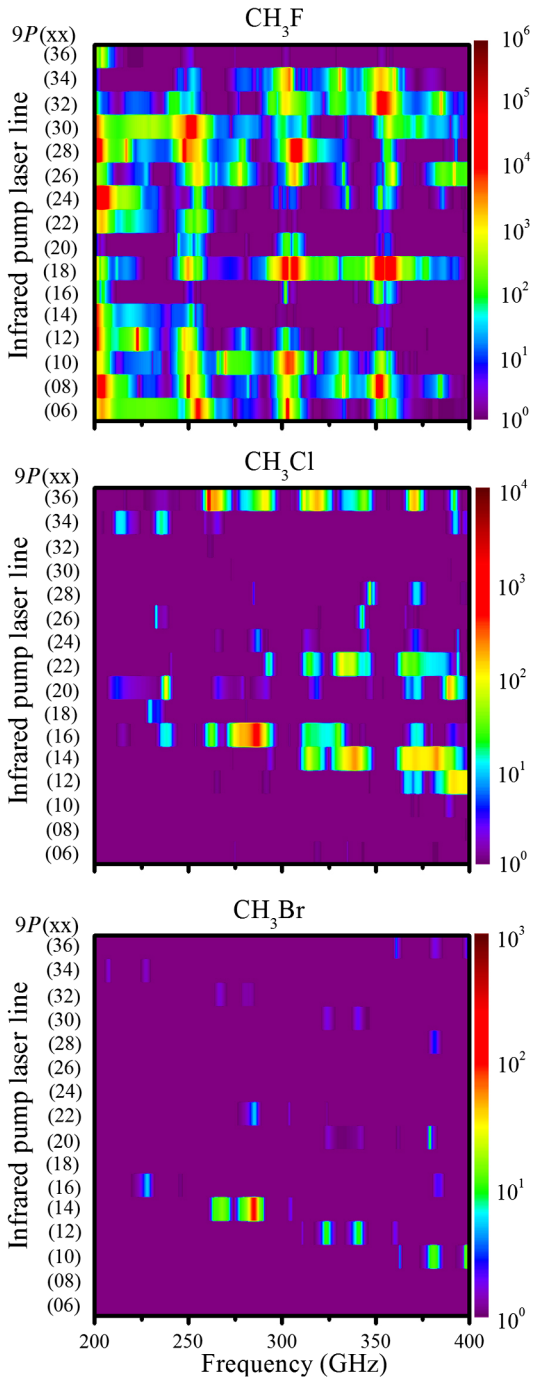

FIG. 8 Plots of $\Xi_{\min}(i)$ for $i = CH_3F$, CH_3Cl, and CH_3Br as a function of pump wavelength and probe frequency.

Figure 8 plots $\Xi_{\min}(i)$ for each analyte i. Looking first at CH_3F, there are several pump-probe combinations that produce $\Xi_{\min}(CH_3F) > 100\,000$, meaning the strongest interferent in the specificity matrix (CH_3Br in this case) must have a concentration more than 100 000 times higher than the concentration of CH_3F to produce an equivalent SNR. The options are fewer for CH_3Cl and CH_3Br, but both have combinations that produce large $\Xi_{\min}(i)$, and these plots represent only a small portion of the entire

specificity matrix. These values for $\Xi_{\min}(i)$ will likely decrease as more molecules are added to the specificity matrix.

Therefore, the procedure for identifying the optimal combination of pump line and probe frequency will identify the DR signatures producing the strongest combination of $\Xi_{\min}$ and SNR for a given scenario. A recognition methodology that confidently identifies a target analyte will likely require measurements on multiple transitions in order to rule out the possibility of a false positive reading from the tail of another analyte. Moreover, the concentration of the target analyte may be confidently ascertained through several corroborative measurements guided by the specificity matrix. It is encouraging that the LRT scenarios dramatically reduce the probability of false positive detection through strong atmospheric attenuation, while the standard scenarios provide strong DR signatures so that confident assignments may be made after only a few strategically selected measurements.

VII. CONCLUSION

The utility of a DR atmospheric sensor for remote detection and identification of trace gases up to 1 km away is quantitatively explored for various atmospheric conditions by establishing power requirements, identifying key sources of noise, and describing concentration detection thresholds for the abundant isotopomers of three prototypical molecules: CH_3F, CH_3Cl, and CH_3Br. Limits in operational probe frequency are ascertained as a function of transceiver and retroreflector size and varying atmospheric attenuation. An analysis of the scenario-dependent spectra reveals the sensitivity of the SNR to molecular parameters, range, and dew point, then quantifies the detection threshold as a function of pump power, probe power, and cloud concentration. The concept of a recognition specificity matrix is also introduced to indicate a measurement strategy for confident identification of analytes and a methodology for estimating the PFPD. The techniques we present here may be extended to any molecule of interest, from which the ultimate utility of IR-THz DR spectroscopy for remote detection may be discerned.

ACKNOWLEDGMENTS

The authors thank S. H. Srikantaiah and J. Hesler for their help with the coincidence and noise calculations, respectively. This work is sponsored by DTRA, DARPA, and U.S. Army competitive in-house laboratory research.

[1] H. S. P. Müller, F. Schlöder, J. Stutzki, and G. Winnewisser, The Cologne database for molecular spectroscopy, CDMS: As useful tool for astronomers and spectroscopists, J. Mol. Struct. **742**, 215 (2005).

[2] J. Bak and S. Clausen, FTIR emission spectroscopy methods and procedures for real time quantitative gas analysis in industrial environments, Meas. Sci. Technol. **13**, 150 (2002).

[3] L. S. Rothman *et al.*, The HITRAN2012 molecular spectroscopic database, J. Quant. Spectrosc. Radiat. Transfer **130**, 4 (2013).

[4] M. D. King, Y. J. Kaufman, P. W. Menzel, and D. Tanre, Remote sensing of cloud, aresol, and water vapor properties from the moderate resolution imaging spectrometer (MODIS), IEEE Trans. Geosci. Remote Sens. **30**, 2 (1992).

[5] S. W. Sharpe, T. J. Johnson, R. L. Sams, P. M. Chu, G. C. Rhoderick, and P. A. Johnson, Gas-phase database for quantitative infrared spectroscopy, Appl. Spectrosc. **58**, 1452 (2004).

[6] I. R. Medvedev, C. F. Neese, G. M. Plummer, and F. C. De Lucia, Submillimeter spectroscopy for chemical analysis with absolute specificity, Opt. Lett. **35**, 1533 (2010).

[7] F. C. De Lucia, D. T. Petkie, and H. O. Everitt, A double resonance approach to submillimeter/terahertz remote sensing at atmospheric pressure, IEEE J. Quantum Electron. **45**, 163 (2009).

[8] D. J. Phillips, E. A. Tanner, F. C. De Lucia, and H. O. Everitt, CH_3Cl Infrared-terahertz double-resonance spectroscopy of CH_3F and at atmospheric pressure, Phys. Rev. A **85**, 052507 (2012).

[9] A. Othonos, Probing ultrafast carrier and phonon dynamics in semiconductors, J. Appl. Phys. **83**, 1789 (1998).

[10] D. Rosen, A. G. Doukas, Y. Budansky, A. Katz, and R. R. Alfano, Time resolved luminescence of photoexcited p-type gallium arsenide by population mixing, Appl. Phys. Lett. **39**, 935 (1981).

[11] A. Högele, C. Gall, M. Winger, and A. Imamoğlu, Photon antibunching in the photoluminescence spectra of a single carbon nanotube, Phys. Rev. Lett. **100**, 217401 (2008).

[12] *Handbook Of Laser Wavelengths*, edited by M. J. Weber (CRC Press, Boca Raton, FL, 1999).

[13] T. Y. Chang and T. J. Bridges, Laser action at 452, 496, and 541 μm in optically pumped CH_3F, Opt. Commun. **1**, 423 (1970).

[14] G. Dodel, On the history of far-infrared (FIR) gas lasers: Thirty-five years of research and application, Infrared Phys. Technol. **40**, 127 (1999).

[15] H. O. Everitt, D. D. Skatrud, and F. C. De Lucia, Dynamics and tunability of a small optically pumped cw far-infared laser, Appl. Phys. Lett. **49**, 995 (1986).

[16] R. L. Crownover, H. O. Everitt, F. C. De Lucia, and D. D. Skatrud, Frequency stability and reproducibility of optically pumped far-infared lasers, Appl. Phys. Lett. **57**, 2882 (1990).

[17] S. -L. Chua, C. A. Caccamise, D. J. Phillips, J. D. Joannopoulos, M. Soljacic, H. O. Everitt, and J. Bravo-Abad, Spatio-temporal theory of lasing action in optically-pumped rotationally excited molecular gases, Opt. Express **19**, 7513 (2011).

[18] T. W. Pape, F. C. De Lucia, and D. D. Skatrud, Time-resolved double resonance study of J- and K-changing rotational collisional processes in CH_3Cl, J. Chem. Phys. **100**, 5666 (1994).

[19] M. I. Skolnik, *Introduction To Radar Systems*, 3rd ed (McGraw Hill, New York, 2002).

[20] F. C. De Lucia, Noise, detectors, and submillimeter-terahertz system performance in nonambient environments, J. Opt. Soc. Am. B **21**, 1273 (2004).
[21] D. M. Pozar, *Microwave Engineering*, 4th ed. (John Wiley & Sons, Hoboken, NJ, 2011).
[22] C. H. Townes and A. L. Schawlow, *Microwave Spectroscopy* (Dover, New York, 1975), p. 413.
[23] U. Pöschl, Formation, and decomposition of hazardous chemical components contained in atmospheric aerosol particles, Journal of aerosol medicine : the official Journal of the International Society for Aerosols in Medicine **15**, 203 (2002).
[24] J. H. Overton, Jr., V. P. Aneja, and J. L. Durham, Production of sulfate in rain and raindrops in polluted atmospheres, Atmos. Environ. (1967) **13**, 355 (1979).
[25] H. Kogelnik and T. Li, Laser beams and resonators, Proc. IEEE **54**, 1312 (1966).
[26] T. Li, Diffraction loss, and selection of modes in maser resonantors with circular mirrors, Bell Syst. Tech. J. **44**, 917 (1965).
[27] G. D. Boyd and J. P. Gordon, Confocal multimode resonator for millimeter through optical wavelength masers, Bell Syst. Tech. J. **40**, 489 (1961).
[28] A. E. Siegman, *Lasers* (University Science Books, Sausalito, CA, 1986).
[29] H. J. Liebe, An updated model for millimeter-wave propagation in moist air, Radio Sci. **20**, 1069 (1985).
[30] P. W. Rosenkranz, Water vapor microwave continuum absorption: A comparison of measurements and models, Radio Sci. **33**, 919 (1998).
[31] W. Gordy and R. L. Cook, *Microwave Molecular Spectra* (Wiley, New York, 1970).
[32] J. O. Hirschfelder, C. F. Curtis, and R. B. Bird, *Molecular Theory Of Gases And Liquids* (Wiley, New York, 1964).